Three-phase Grid Connected Modular-Multilevel Converter Fed by Proton Exchange Membrane Fuel Cell

M. Priya* (iD), P. Ponnambalam**‡ (iD)

*School of Electrical Engineering, Vellore Institute of Technology, Vellore, Tamil Nadu, India

** School of Electrical Engineering, Vellore Institute of Technology, Vellore, Tamil Nadu, India

(murthypriya.eee@gmail.com, p.ponnambalam@gmail.com)

‡P. Ponnambalam; Tel: +919894777845, p.ponnambalam@gmail.com

Abstract- Modular-Multilevel Converter (M-MC) is an effective method of integrating non-conventional energy sources with grid electricity. In the current scenario, fuel cells have been made the best choice by providing a constant voltage and current density with constant load draw in the field of distributed energy sources. A power converter can be used to adjust the fuel cell output voltage to compensate for expected power spikes or meet the load requirements. This paper provides the first attempt to examine the impact of M-MC system behaviour on the Proton Exchange Membrane Fuel Cell (PEMFC). The proposed PEMFC-based grid-connected M-MC control method is evaluated. A decoupling controller is used to ensure the interfaced system's stability of M-MC. An analysis is carried out for the grid-connected M-MC for the PEMFC system to mitigate the harmonics. The result shows that the capacitor voltages in the Sub Module (SM) are balanced, with a peak voltage ripple of 12.5% from the DC bus voltage regulation. The harmonics of the circulating current have a peak value of about 30% of the peak arm current. As a result, a pure sinusoidal arm current waveform is obtained as the distortion is mitigated. To accomplish independent active power distribution, an effective control system for active power extraction and voltage distribution is designed. The performance of the proposed system for 6kW PEMFC at different operating temperatures is tested using the hardware in the loop (HIL) simulation with the help of real-time simulator OP5700 to verify the feasibility.

1. Introduction

With the improvement of renewable energy sources (RES), integration research of Grid energy and fuel cells have accelerated drastically in research and feasible knowledge due to growing electricity demand, reduced fossil fuel consumption, and environmental concerns[1]. Fuel cells, photovoltaics, and wind turbines are the most promising renewable energy generation technologies[2][3]. The power ratings of fuel cells used in renewable energy implementations vary from 500 W to 1 MW, depending on the application region [4]. PEMFCs are predominantly used to offer electric energy in both grid-connected and stand-alone modes to minimize application-fed electrical consumption at nearby masses[5]. Consequently, those cells are linked to the electric grid through an interfacing between the power electronic converters [6][7]. In the grid interconnection of fuel cells, these issues could result in irregular switching, overheating, and hardware damage [8][9]. The rapid advancements of high-voltage (HV) and high-power (HP) switching devices have a significant impact on Power Electronic (PE) technology in power networks [10]. Furthermore, dc collection and transmission systems outperform ac systems in terms of performance, losses, and costs. As a result, PE converters are in high demand in this industry.

Besides, for medium and high-power applications, the M-MC is becoming a prominent multilevel-converter topology [11]. Lesnicar and Marquardt [12] proposed their M-MC concept in 2002, and they designed modular topologies. M-MC power converters are characterized by high modularity, low harmonic distortion, highly efficient, and scalable[13]. On the contrary, it has also encountered issues such as circulating-current and imbalanced voltage between the SMs [14]. In a smart home setting with fuel cells, photovoltaic generating, energy storage, and electric car recharging, an M-MC is used as the interface with the power grid [15]. To test its viability for grid connection, PEMFC is analyzed with varying air supply while maintaining constant fuel supply and

varying fuel supply pressure while maintaining constant air supply in [7].

The [10] has used a 5kW PEMFC for a direct current constant load in a grid-connected arrangement, with a focus on Low-Frequency (LF) 100 Hz noise (current ripple), which has a substantial effect on fuel cell efficiency and lifetime. Due to its inherent damping feature, the converter side current feedback approach was utilised in [16] to interface the PEMFC system into the weak power distribution network via an LCL filter in effort to examine the quality of the injected power. In [17], a complete evaluation and assessment of the effects of LF current ripple and harmonics on PEMFC performance and durability is carried out, as well as the implementation and testing 300 W PEMFC stack of a Horizon.

In [18], the M-MC is integrated to RES & grid, and they have proposed dynamic and steady-state analysis in order to reduce the second harmonic content of the circulating currents, and to decrease the capacitor voltage fluctuation. The [19] proposes multi-hierarchy control for M-MC under unbalanced grid conditions, as well as arm current control. In [20], the comprehensive dynamic-phasor based state-space model of M-MC is presented and a comparative analysis of operational stability by using AC-voltage-control mode and reactive-power-control mode of the M-MC-HVDC station is performed. The M-MC converter topologies of Voltage-Source Control (VSC) and Current-Source Control (VSC) were studied in depth in [21]. Apart from that, HP uses of the HVDC system are discussed. The CSC, on the other hand, has several major flaws, including the filter's size, poor AC networks, DC and AC side harmonic distortions, and the inability to build a multi-terminal connection. In [22], M-MC is integrated with PV and grid using level-shifted PWM to find disturbance under solar irradiations, here the arm inductors are switched by a transformer that contains the complexity of the circuit. A selective virtual loop mapping modulation method is used in M-MC for PV grid connection [23] to achieve dynamic capacitor voltage balance.

According to the above-mentioned literature review, grid-connected three-phase M-MC technology utilising PEMFC is lacking in the literature. Hence, in this paper, a three-phase M- MC control-based grid-connected PEMFC is designed and controlled to investigate the system behaviour in grid configuration by using decoupled current control strategy. The M-MC control approaches have three objectives, one PEMFC control using Maximum Power Point Tracking (MPPT), second, relating to the application and third, to the control of M-MC itself, which are subdivided as (a) following the output current (or power), (b) mitigating the circulating currents, and (c) controlling the SM capacitor voltages. To have accurate results, the decoupling current control strategy could be used to compute the inner M-MC variables. This research article focuses on grid-connected PEMFC for three-phase M-MC configuration under different temperature variations. In M-MC the circulating current is controlled by synchronous reference dq-frame and the submodule capacitor voltage are controlled by average voltage control. The performance under different operating temperature for PEMFC is analyzed and integrated into M-MC.

The system configuration of Grid-connected M-MC fed PEMFC is specified in Section 2. Section 3 handles the M-MC system overview and mathematical operations followed by control of MMC in which the following are taken into consideration (i) choosing the appropriate control variable for DC bus voltage, (ii) SM capacitor voltage control and (iii) circulating-current control. Section 4 depicts the real-time simulation results and discussion. The conclusion is formulated in section 5.

2. System Configurations: Grid-Connected M-MC Fed PEMFC

Electrical power is provided by a fuel cell-built power plant, which must be delivered to a distribution location. While the generated dc power on the FC side will not be able to be directly distributed to the electric system. Thus, the fuel cells are linked to the grid interface through PE converters and electrical components. Generally, the interfacing components are 6kW PEMFC, dc-dc boost converters, three-phase M-MC (dc-ac converters), inverter-side output filter, and grid. Generally, a boost converter will be used to boost the PEMFC's output voltage. This output voltage leans to decrease as more current is needed from the cell. Thus, a control system is required to control the output voltage by controlling the boost converter using the MPPT algorithm to extract maximum available power from PEMFC. LCL filters are used in power converters with rectifier input stages to reduce absorbed harmonics. The LCL filter is commonly used in distribution system grid connections. Through the dc-dc boost converter, the PEMFC's DC bus output voltage is coupled to the three-phase M-MC. It's critical to be able to adjust and step-up fuel cell voltage. The PEMFC and three-phase M-MC to grid interface system modelling is detailed in the next section. The grid-connected M-MC based PEMFC is depicted in Figure 1.

2.1 PEMFC And Dc-Dc Boost Converter Configuration

An electrochemical reaction in a fuel cell converts the chemical energy of a fuel into electrical energy, resulting in the generation of electricity. Fuel cells provide an alternate efficient, non-polluting power source that produces no noise and has no moving parts [24]. In an electrochemical reaction, fuel cells utilize hydrogen as such fuel and oxygen (usually
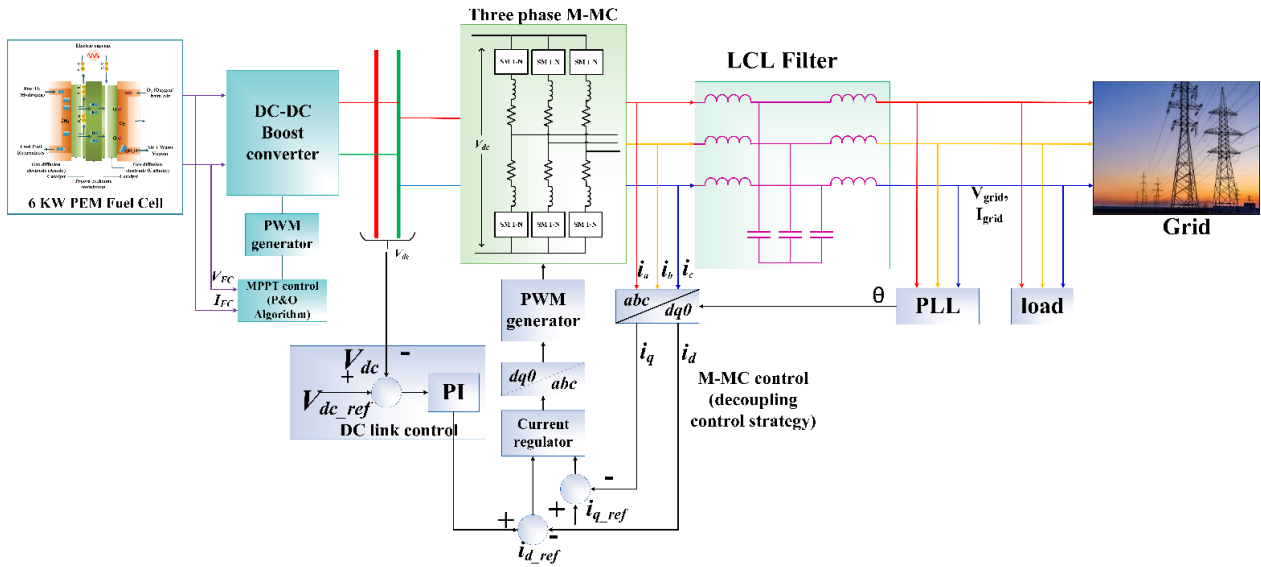
Fig 1. Structure of grid-connected M-MC fed PEMFC

from the air) as the oxidant [6]. As a result of the reaction, electricity, water, and heat are produced as by-products. When hydrogen gas is introduced into the system, the Protons pass through the membrane and react with oxygen in the surrounding environment (forming water). Because electrons are unable to travel through the membrane, they must circumvent it, resulting in a DC electrical source [25][26]. There are three types of losses in the FC: ohmic loss, activation loss, and concentration loss. The terminal voltage of the PEMFC stack is represented in [27] if n cells are combined. The potential difference between the terminals and PEMFC under the conditions of these losses can be defined in [27],[28]. The detailed mathematical modelling of PEMFC is discussed in[29],[30],[31].
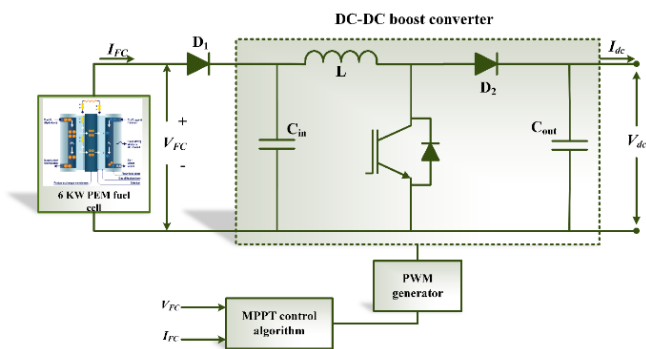

Fig 2. PEMFC and dc-dc boost converter

The provided output voltage to the load can be regulated to the required voltage using a boost DC-DC converter. The duty cycle (d) of the boost DC-DC converter can be changed to control the output voltage. When the switch is closed, the diode's bias is reversed. Kirchhoff's voltage law

is applied to the path that contains the Fuel Cell, inductor, and closed switch.

$$V_L = V_{FC} \qquad (1)$$

When the switch is opened, the inductor current cannot change instantly, therefore the diode becomes forward biased to provide an inductor current path. Assuming a constant output voltage V_O, the voltage across the inductor is

$$V_L = V_{in} - V_O \qquad (2)$$

For periodic operation, the average inductor voltage must be zero. The average inductor voltage over one switching period is expressed as

$$V_L = D(V_{in}) - (1 - D)(V_{in} - V_O) = 0 \qquad (3)$$

$$V_0 = \frac{V_{in}}{(1 - D)} \qquad (4)$$

The average duty cycle D is the time relationship between when the switch is turned on and when it is turned off in respect to the overall switching period. The gain ratio between output and input voltage can be evaluated at steady state using equation (4):

$$M = \frac{V_0}{V_{in}} = \frac{1}{(1 - D)} \qquad (5)$$

When a fuel cell is directly linked to an external load, its output power affects both the internal electrochemical process and the external load impedance [6]. The PEMFC output power is not constant and differs significantly about partial pressures of cell temperature, hydrogen, membrane

water content, and oxygen gas. The PEMFC dc-dc converter with MPPT controller is as illustrated in Figure 2. The design specifications of dc-dc boost converter are given in Table 1. Perturb and Observe (P&O) is the most commonly used MPPT algorithm due to its ease of implementation. This algorithm is utilized to find the maximum power point and calculates the PEMFC actual power and measure voltage and current. The P&O algorithm can predict when the operating voltage is approaching maximum power point voltage by comparing the actual and the preceding state of power and voltage [29][32]. If there is still an increase in power, the MPP will remain the same, and vice versa.

Table 1. Design specifications of dc-dc boost converter

Parameter Description	Rating
Switching frequency (Fs)	$5000Hz$
Inductor (L)	$5mH$
Capacitor (C_{in})	$200\mu F$
DC link capacitor (C_{Out})	$3200\mu F$

3. M-MC System Overview

3.1 Structure of M-MC

To achieve the desired device voltage while generating a multilevel output voltage waveform of high-quality, it uses a cascade connection of submodules [33]. Figure 3 depicts the grid-connected mode of a three-phase M-MC dc-ac converter. The SM is a component of the M-MC that can be designed in a variety of ways using IGBT devices and DC capacitors. During normal M-MC operation, SMs are regulated to generate the necessary AC voltages[34]. SM can be considered a controllable source of voltage. Of all possible SM circuit topologies, the half-bridge circuit or a chopper cell is the most prominent[35]. This is owing to the massive energy expenditure as well as the low number of components in the above-mentioned SM.

To minimize the current owing to the instantaneous voltage differential between the arms, the arm inductor is linked in series with each set of submodules [36]. Likewise, during a DC-side short circuit fault, the arm inductor suppresses the fault current by supplying low di/dt [37]. On the contrary, to model the each arm of the M-MC endures power losses, the arm resistor is used [38].

In this configuration, each converter phase is called a phase leg. Each phase leg consists of one upper-arm 'u' (i.e., Positive-arm) and one lower-arm 'l' (i.e., Negative-arm)
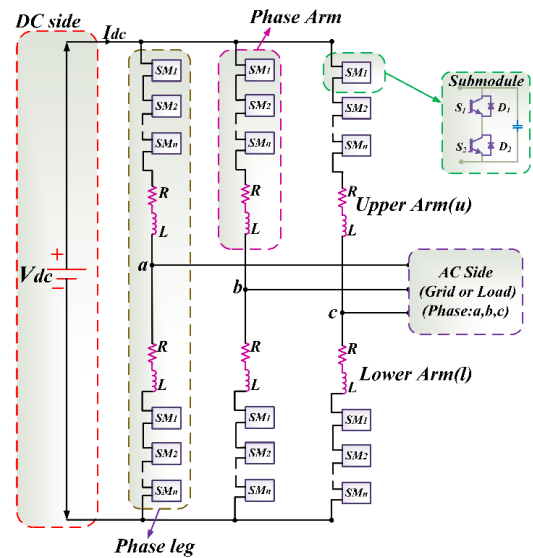

Fig 3. Three-phase M-MC structure

connected between the dc terminals with a voltage $\frac{Vdc}{2}$ as a split-up DC source. Each arm has a group of submodules (i.e., 'N' series-connected, technically identical HB-SMs, an inductor (l) and resistor(r).

3.2 Mathematical Modelling Of M-MC

Modelling of M-MC could become complex and, due to many cells, Its simulation could take a long time. Several approaches were suggested in the literature as a means of simplifying its model to mitigate this issue. The easiest is to consider as a single equal voltage source each arm's power cells as shown in Figure 4(b).

An M-MC converter with N SMs per arm can generate a phase to midpoint of the DC voltage with N+1 levels. The number of AC output levels can be increased by increasing the number of SMs.

The sum of the number of SMs in the ON state in the upper n_{up} and lower n_{low} arms of each phase is equal to the number of SMs per arm n. The SMs for each arm consist of $n = 4$.

$$n_{up} + n_{\text{low}} = N \quad (6)$$

During the activity of the M-MC, the arm current moves through the SM capacitors, which charges and release the capacitors. The DC transport voltage Vdc is similarly dispersed between all the SMs. To ensure the proper process of the converter, the SM capacitor voltages should be directed to the below reference value.

$$V_c^* = \frac{Vdc}{N} \quad (7)$$

Pertaining the Kirchhoff's voltage law to the loop linking the points for both upper and lower arms (midpoint voltage of dc bus (m)-positive arm (p)- midpoint of converter phase leg- midpoint voltage of dc bus) and (midpoint voltage of dc bus (m)-negative arm (n)- midpoint of converter phase leg- midpoint voltage of dc bus). The expression leads to:

$$V_{u,abc} = \frac{Vdc}{2} - V_{g,abc} - L\frac{di_{az}}{dt} - Ri_{az} \qquad (8)$$

$$V_{l,abc} = \frac{Vdc}{2} + V_{g,abc} - L\frac{di_{az}}{dt} - Ri_{az}$$

Where, $V_{u,abc}$ is $\{Vau, Vbu, Vcu\}$ represents the upper-arm and lower-arm voltage respectively, $V_{g,abc}$ is $\{Vga, Vgb, Vgc\}$ are three-phase grid side terminal voltages with respective to the neutral point V_N, i_{az} is (i_{au}, i_{al}) are the upper and lower-arm currents, L is the arm inductance, R is the resistance of inductance, Vdc is the DC link voltage. While Kirchhoff's current law is utilized to the positive and negative connections of the M-MC arm, the result is as follows:

$$Idc = i_{au} + i_{bu} + i_{cu} = i_{u,abc} \qquad (9)$$

$$Idc = i_{al} + i_{bl} + i_{cl} = i_{l,abc}$$

Each phase of the M-MC has a circulating current that does not appear at the converter's output. A DC component as well as AC components forms the circulating current. The DC component is required for the converter's operation. For each of the arms, a current (upper i_{au} and lower i_{al}) is circulated equally to half the phase current i_a,

$$i_{au} = \frac{i_a}{2} + \frac{Idc}{3} + i_{az} \qquad (10)$$

$$i_{al} = -\frac{i_a}{2} + \frac{Idc}{3} + i_{az}$$

The three-phase side terminal currents are represented by i_a, i_b, i_c. The circulating currents in phase units a,b, and c are i_{az}, i_{bz}, i_{cz}, defined as:

$$i_{az} = \frac{i_{au} + i_{al}}{2} - \frac{Idc}{3} \qquad (11)$$

Where the dc current is distributed proportionally among the three converter legs, and ac current is distributed equally among the two-leg sides. On both arms of the leg, the circulating-current is the same since, this current flows inside the converter, and is expressed as:

$$i_{az} + i_{bz} + i_{cz} = 0 \qquad (12)$$

The ac and dc voltage bus of M-MC can be achieved by deducting and adding up the two equations which are shown from equation (2) respectively. By ignoring the voltage drop through the arm impedance given as:

$$\begin{cases} V_{g,abc} = \frac{1}{2}(V_{au-}V_{al}) \\ Vdc = V_{au-}V_{al} \end{cases} \qquad (13)$$

The above equation shows that the arm voltages have significant impact on the input ac-side and output dc-side voltages of M-MC circuit.

3.3 M-MC Grid Interface Control

The control of M-MC as shown in Figure 4, consists of AC side control, DC voltage control, SM capacitor voltage, output currents, ac voltage control and circulating current control. The DC link voltage is regulated with an outer control loop of the converter, allowing the balance of active and reactive power delivered to the electrical network. A voltage balance control algorithm and a leg voltage control are part of the SM capacitor voltage control. The voltage balance approach ensures that the submodule capacitors receive the same voltage from inside the arm. Power quality and current harmonic correction are handled by the decoupled current control technique. A Phase Locked Loop (PLL) device is also used to generate a synchronised reference current for the present control loop.

3.3.1 Control of AC Side

The control of AC side is intended to accomplish the total submodule capacitor voltage stable and unity power factor. Cascade control with SM voltage control loop and inner control loop is used to achieve this control. The inner control is designed based on decoupling current control with d-axis i_d^* and q-axis i_q^* as illustrated in figure 4(a). This control loop relates the submodule voltage regulator V_c^* and the calculated mean value $V_{c,avg}$ to estimate the value of i_d^*. The dq-axis current sources with their calculated values id and iq have been handled by current regulators. These output values are given to the inverse dq transformation to produce compensating voltage V_{abc}^*. These voltages help to stimulate required three-phase leg input currents.

3.3.2 Control of DC Bus Voltage

The dc side control maintains a consistent dc link voltage while also balancing capacitor voltages. Two outside voltage loops and one interior dc current loop are employed in cascaded control to achieve this performance. One outside voltage loop is created by measured value Vdc and dc bus voltage reference V_{dc}^*. A voltage regulator measures these signals to calculate the dc link current reference idc, It is utilised to calculate each phase leg's current reference. The dc bus voltage control loop is as shown in figure 4 (c).
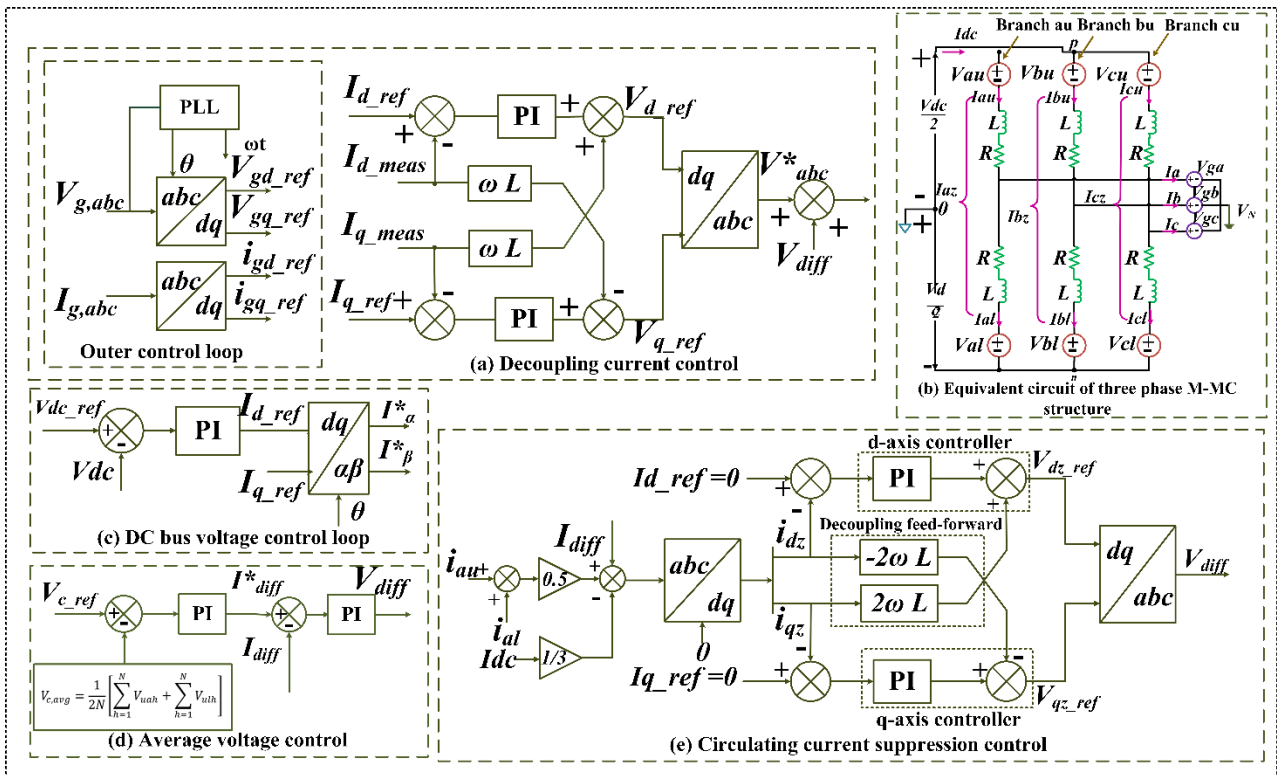
Fig 4. Control of M-MC grid interface

3.3.3 *Control of SM Capacitor Voltage*

The operational voltage of M-MC could be enhanced by linking more SMs in series in each arm. The voltages of these SM must be kept constant because they have floating capacitors. Controlling the voltage of SM capacitors is essential for achieving high-efficiency current control, improving output power quality, and ensuring stable and controllable activity. To produce the appropriate voltage level, the voltage balancing technique chooses a particular number of SMs from an arm's N submodules. As a result, the balancing technique is also known as the submodule selection process. The leg voltage control controls the average of $2N$ submodule capacitors voltage at a constant value of $V_{c,avg}$. The measured average voltage of each leg is given by:

$$V_{c,avg} = \frac{1}{2N}\left[\sum_{h=1}^{N} V_{uah} + \sum_{h=1}^{N} V_{ulh}\right] \quad (14)$$

Where V_{uah}, V_{ulh} are the SM capacitor voltages in the upper-arm and lower-arm of the converter leg. The average voltage control is as shown in figure 4(d).

An outer loop with a proportional-integral (PI) controller is used to control the entire capacitor voltage in every arm. The PI controller $(k_{pv} and\ k_{iv})$ controls the number of capacitor voltages in each arm to be equal to the DC-bus voltage. The overall capacitor voltage in each arm is regulated through an outside loop with a proportional-integral (PI) controller. The PI controller i_{diff}^* regulates the sum of all capacitor voltages in an arm to be equal to the DC-link voltage, resulting in:

$$i_{diff}^* = k_{pv}\big(V_c^* - V_{c,avg}\big) + k_{iv}\int \big(V_c^* - V_{c,avg}\big)dt \quad (15)$$

To study the behaviour of M-MC system, the gain values of (Kp and Ki) are taken from [39].

3.3.4 *Circulating Current Control*

Circulating currents are internal currents that flow between the converter's arms but not outside of them, and are produced by M-MC. The voltage differential between the upper and lower-arms of the converter legs is used to calculate these currents. The capacitor voltage ripple is a single source of circulating currents with twice the output frequency. The circulating current has no effect on the AC output voltages and currents. Inadequate circulating current control, on the other hand, raises the arm current peak/RMS value, affecting the submodule capacitor voltages ripple, device power losses, and device rating. In the synchronous dq frame, the circulating currents become DC signals. Simple PI-regulators can be used to control the DC signals.

From equation (2) and (5), the common-mode current elements are given by,

$$L\frac{di_{az}}{dt} + Ri_{az} = \frac{Vdc}{2} - \frac{1}{2}(V_{au} + V_{al}) - R\frac{Idc}{3} \quad (16)$$

The circulating currents mainly comprise harmonic elements of even order. The second and fourth-order harmonic components are dominant between them. Since there is no steady-state error in these harmonic components, those are difficult to detect with a PI controller. As a result, $Tabc$ and dq transformation matrices, time-varying signals are converted to DC signals. The above equation can be used to compute the three-phase circulating current pattern in the stationary abc frame:

$$\begin{bmatrix} V_{az} \\ V_{bz} \\ V_{cz} \end{bmatrix} = L\frac{d}{dt}\begin{bmatrix} i_{az} \\ i_{bz} \\ i_{cz} \end{bmatrix} + R\begin{bmatrix} i_{az} \\ i_{bz} \\ i_{cz} \end{bmatrix} \quad (17)$$

The synchronous dq frame control device is utilized to reduce the second-order harmonic after the circulating-currents. The following is a synchronous dq frame rotating at -2ω frequency is:

$$\begin{bmatrix} V_{dz} \\ V_{qz} \end{bmatrix} = L\frac{d}{dt}\begin{bmatrix} i_{dz} \\ i_{qz} \end{bmatrix} + \begin{bmatrix} 0 & -2\omega L \\ 2\omega L & 0 \end{bmatrix}\begin{bmatrix} i_{dz} \\ i_{qz} \end{bmatrix} + R\begin{bmatrix} i_{dz} \\ i_{qz} \end{bmatrix} \quad (18)$$

At This Point, 2ω is double the system angular frequency. both the dq-axis components are forced to zero in the control to suppress the circulating currents completely and is expressed as:

$$\begin{cases} i_{qz}^* = 0 \\ i_{dz}^* = 0 \end{cases} \quad (19)$$

To control the dq-axis, the PI controller will be used to control and forced to follow their respective reference values. At the reference value, i_{dz} and i_{qz} synchronizes the current control which is denoted by i_{dz}^* and i_{qz}^* to adjust the output reference voltage of the converter. The reference voltage V_{dz}^* and V_{qz}^* are converted back to three-phase using inverse transformation and gives V_{abc}^* respectively. To result in the circulating suppression current, the total reference voltage is required to generate the output voltage of M-MC. Figure 4(e) depicts the control diagram for circulating current control.

4. Real-Time Simulation Results and Discussions

The definite structure is emulated in MATLAB / SIMULINK and verified using the Real-Time simulation domain for the operation of system operation and control of M-MC in the power system. The HIL setup is as shown in Figure 5. The overall system presented in Figure 1 is a built-in RT lab simulation that has been dumped into the OP5700 real-time HIL simulator to verify system performance. The M-MC system control and PEMFC model parameter values

are tabulated in Table 1. The active power distribution and control of three-phase M-MC with PEMFC temperature variation are analysed by using decoupled current control strategy. PEMFCs operate at a low temperature of about 80 degrees Celsius (353.15K) low-temperature operation allows them to start quicker (with shorter warm-up time) and decreases stress on system components, resulting in higher reliability.
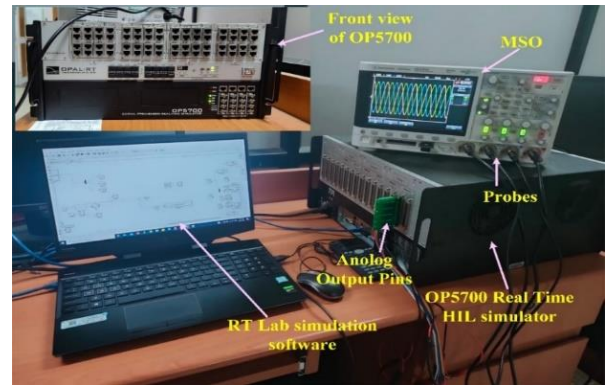

Fig 5. Real-time HIL setup

Table 2. overall system parameter values

M-MC and control parameter values	
System Parameters	Values
DC bus voltage (Vdc)	500V
Line to line (RMS) voltage of ac side (V_{LL})	220V
Number of SM per phase (N)	8
Submodule capacitor voltage (V_C)	62.5V
Maximum output power (p)	6kW
Cell capacitance (C)	6mF
Arm inductance (L)	1.75mH
Arm resistance (R)	0.5Ω
Fundamental frequency (f)	50Hz
Carrier frequency (fc)	5kHz
M-MC side filter inductance (Lc)	2.2mH
Grid side filter inductor (Lg)	1.5mH
Capacitor filter (Cf)	13μF
PEMFC model parameters	
Rated power	6KW
Nominal operating voltage	45V
Nominal operating current	133.3A
Number of cells	65
Nominal airflow rate	300 lpm
Hydrogen partial pressure	1.5 bar
Oxygen partial pressure	1 bar
Temperature	298K

Case 1: PEMFC at different operating temperature. The power produced in an FC-based system is dependent on pressure control, water and heat management, hydrogen, and oxygen flows. One of the basic process factors is reactant utilisation, which is related to the fuel cell stack current. Whenever a load is attached to a fuel cell system, the control system must manage the hydrogen flow rate to prevent FC voltage degradation. In this case, the power generated from the PEMFC at three different operating temperatures is considered which are $332K, 200K$ and $289K$. Figure 6 shows the PEMFC at different operating temperatures. At temperature $T = 332K$, the power generated from PEMFC is 7kW, with the fuel cell voltage of 52V and the current is 133.07A at the period of t_0 to $t_1 sec$. From t_1 to $t_2 sec$, 30V is generated, the current is 133.07A and the power generated from PEMFC is 4kW at the temperature of $T = 200K$. then, from the period of t_2 to $t_3 sec$, 45V and 133.3A of current is generated, then 6kW of power is generated from the PEMFC at the temperature of $T = 298K$. The fuel cell stack voltage, current, power generated at different operating temperature is as displayed in Figure 7.
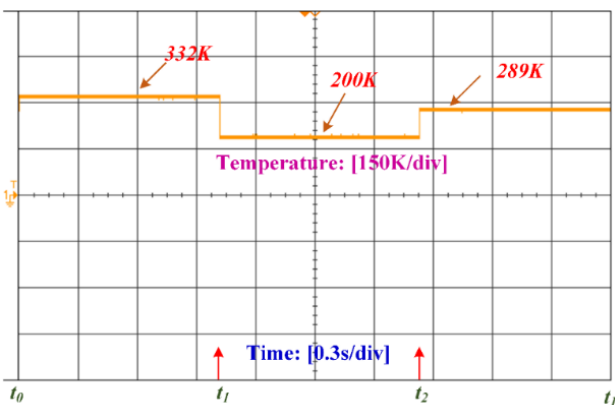

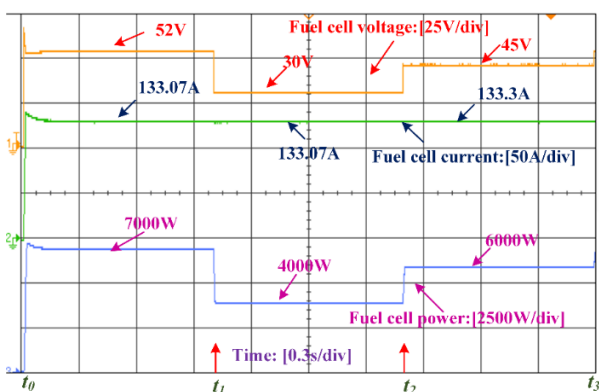**Fig 6.** PEMFC at different operating temperature.

Fig 7. Fuel cell voltage, current, power at different operating temperature.

The boost converter controls and adjusts the output power of the fuel cell. he boost converter receives the uncontrolled output voltage from the fuel cell. The PI controller adjusts the MPPT duty ratio of the converter to supply the required output voltage despite changes in hydrogen flow rate, load, or fuel cell operational parameters. The maximum output voltage is generated from the PEMFC boost converter to provide the constant DC bus voltage of 500V. At $T = 332K$ the generated dc link power is 7kW and 14A of dc link current at the period of t_0 to $t_1 sec$. At $T = 200K$ the generated dc link power is 4kW and 8A of dc link current at the period of t_1 to $t_2 sec$. At $T = 298K$ the generated dc link power is 6kW and 12A of dc link current at the period of t_2 to $t_3 sec$. The fuel cell DC-link output waveforms generated at different operating temperature is as illustrated in Figure 8.
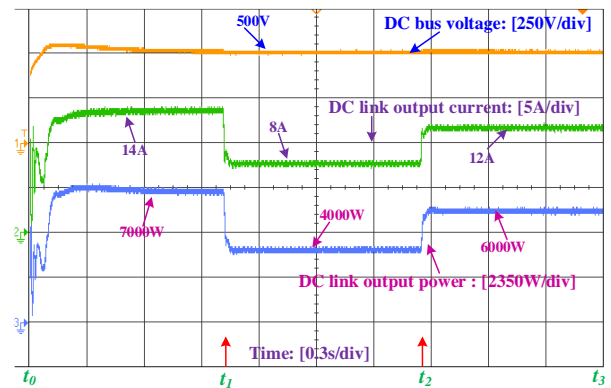

Fig 8. Fuel cell dc bus voltage, dc-link current, dc link power

Case2: Regulation of SM capacitor voltage. 9(a), (b), (c) depicts the upper and lower-arm of the individual SM capacitor voltage. By balancing the voltages of individual SM capacitors, a sorting method has been developed to maintain the voltages of individual SM capacitors in M-MC. These sorting methods may result in an extremely irregular switching frequency between the SMs, following in larger converter losses in this situation. The average capacitor voltage controller is responsible for ensuring that the M-MC leg evenly distributes the incoming dc-current, and the leftover voltage of each leg's SM capacitor equals the average voltage value. The average SM capacitor voltage for each phase is shown in Figure 9(d). When a load is introduced to the grid, the voltages of SM capacitors fluctuate from their stable values. The voltages are at a tolerable level, are properly balanced, and the voltage fluctuation has been significantly reduced. With a peak voltage ripple of 62.5V at the base frequency, the SM capacitor voltages are balanced.
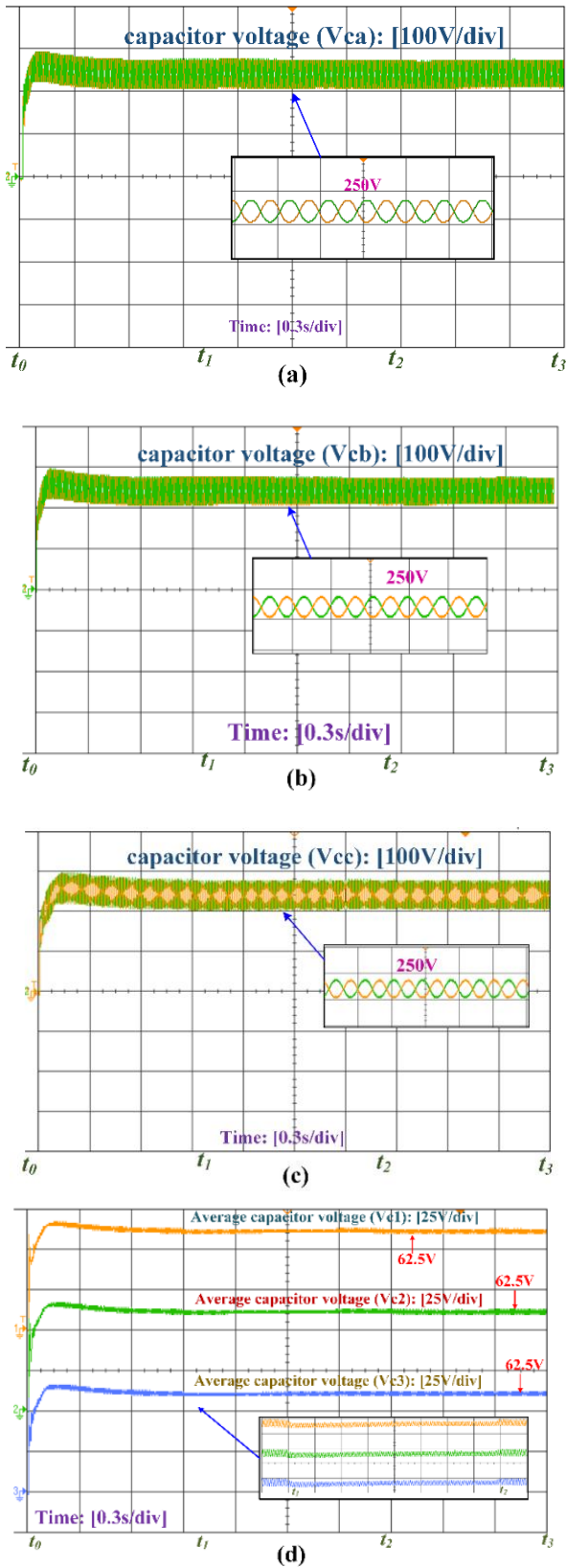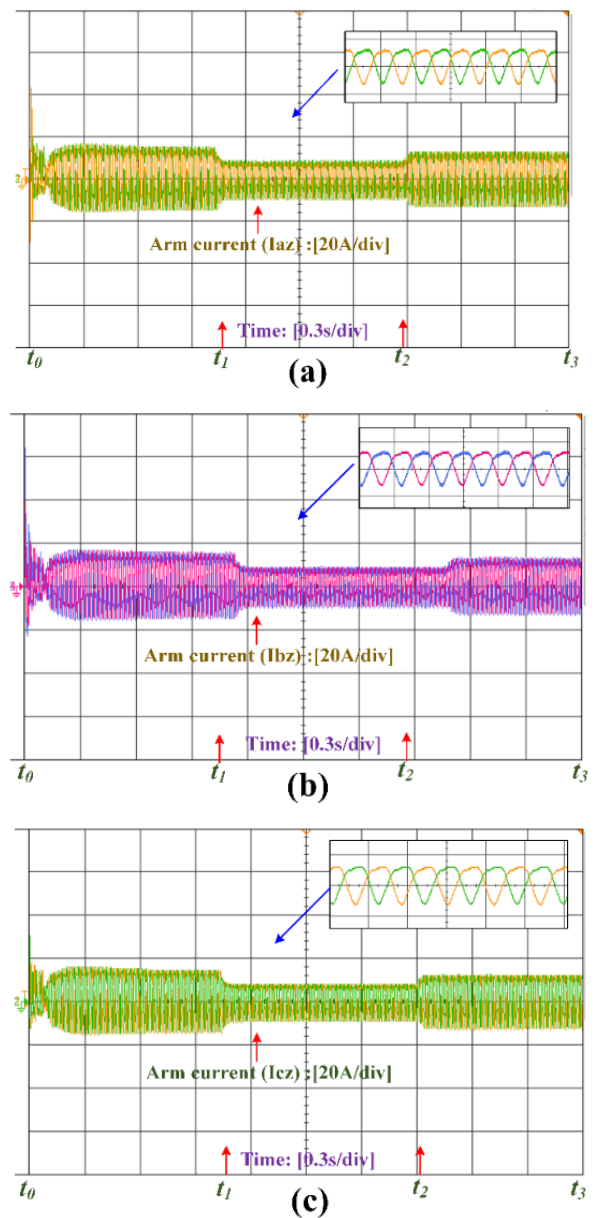
Case 3: M-MCs Arm currents and circulating current. Figure 10 shows currents for each phase (i_{az}, i_{bz}, i_{cz}) of the upper-arm and lower-arm which mainly contains the basic component without harmonics. The circulating current has dc and ac components in the same flow, which causes the arm currents to be distorted. DC-side current divides equally among the three phases and improves the power balance in capacitors. The dc component of the arm current must be included since it illustrates active power transmission between the ac and dc sides. Figure 14 depicts the output of circulating current in the synchronous dq frame. The peak value of the second-order harmonic of circulating current is approximately 3A, which is almost half the peak arm current. As the distortion is reduced, a better (pure sinewave) sinusoidal arm current waveform can be created using this approach.

Fig 9 (a) individual SM capacitor voltage Vca for each phase, (b) individual SM capacitor voltage Vcb for each phase, (c) individual SM capacitor voltage Vcc for each phase, (d) Average SM capacitor voltage $Vc1, Vc2, Vc3$ for each phase.
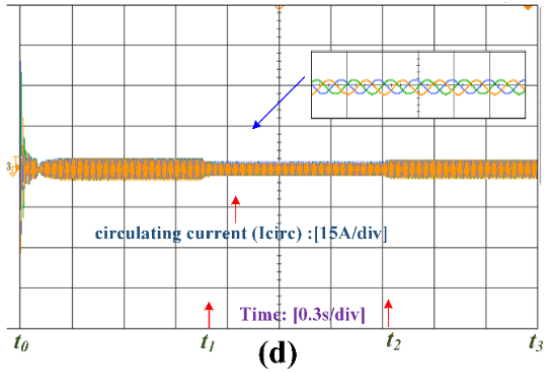
474

Fig 10: (a) M-MC arm currents i_{az} of each phase, (b) M-MC arm currents i_{bz} of each phase (c) M-MC arm currents i_{cz} of each phase, (d) M-MC circulating currents.

Case 4: The behaviour of a PEMFC system in a grid-connected M-MC configuration. Figure 11(a),(b) represents the three-phase output voltage and current of the M-MC. A 6kW PEMFC system was tested using a grid-connected setup. The load on the dc side for both tests was kept constant at 5kW (grid-connected and dc constant load). The M-MC converts the dc power, which was generated from the PEMFC with a voltage rating of 45V, into ac power.
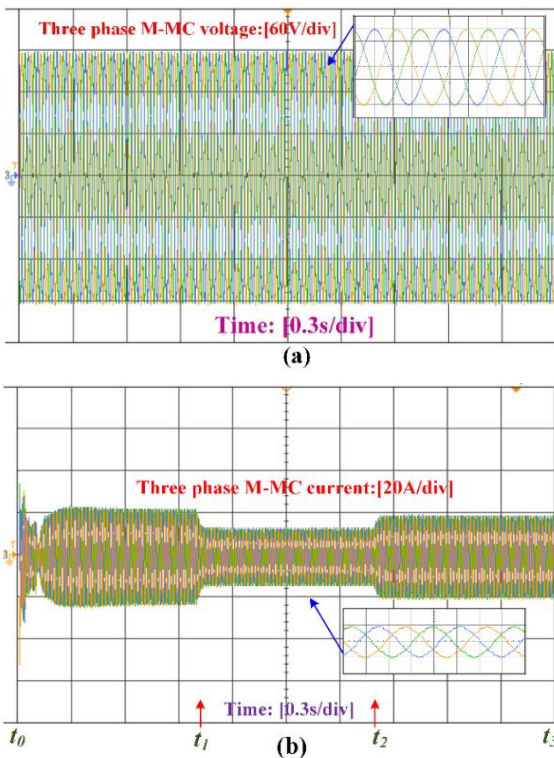
The power obtained from the LCL filter (getting the input from M-MC) is well-filtered, the sizing of capacitor values and designing of dq frame loops allow us to eliminate harmonics that could interrupt the operation of the power generation system. Voltage waveforms were made effectively smooth by applying the correct current control technique. Here, the PI controller is used to control the current flow by taking the feedback current from the load. Figure 11(c), (d) shows that the grid voltage and grid current are in phase, resulting in the injected power having a unity power factor.
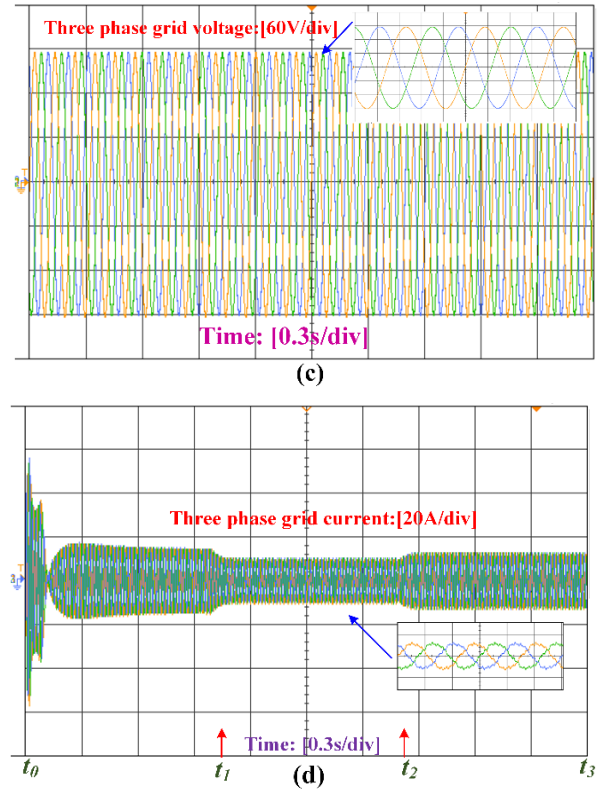

Fig 11 (a) Three-phase M-MC output voltage, (b) Three-phase M-MC output current, (c) Three-phase grid output voltage (d) Three-phase grid output voltage grid current.

Figure 12 depicts the output of M-MC side active power, grid side power and load side power of the PEMFC system. At the period of t_0 to $t_1 sec$, 6.6kW of active power is fed as input from PEMFC to M-MC side from which, 1.6kW of power is injected into the grid side, then 5kW of power is consumed by the load. At the period of t_1 to $t_2 sec$, 3.65kW of active power is fed as input from PEMFC to M-MC side from which 1.35kW of power is fed in the grid side, then 5kW of power is consumed by the load. At the period of t_2 to $t_3 sec$, 5.4kW of active power is fed as input from PEMFC to M-MC side from which 400W of power is injected into the grid side, and then 5kW of power will be consumed by the load. The comparison of the overall system output parameter is analysed and tabulated in Table 2. The control system of the PEMFC based grid-connected M-MC configuration with the designed parameters under different operating temperature is successfully analysed.
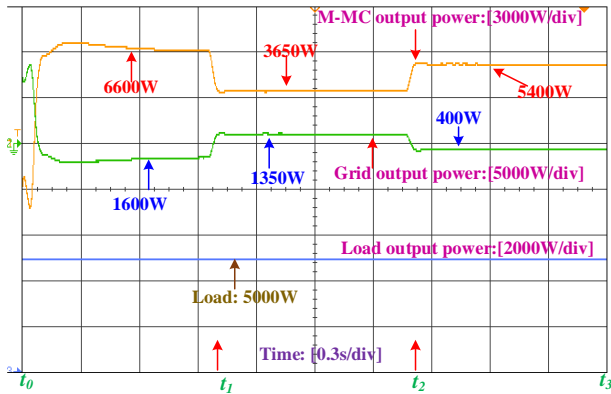
Fig 12. M-MC side, grid side and the load output of active power

Table 3. comparison of overall system output parameters

Indices		PEMFC system behaviour in grid-connected configuration output parameter values		
Time duration (sec)		t_0 to t_1 (0 − 1sec)	t_1 to t_2 (1 − 2sec)	t_2 to t_3 (2 − 3sec)
PEMFC Temperature (K)		332K	200K	298K
PEMFC stack inputs	Input voltage (V)	52V	30V	45V
	Input current (A)	133.07A	133.07A	133.3A
	Input power (W)	7kW	4kW	6kW
PEMFC DC link outputs	output voltage (V)	500V	500V	500V
	output current (A)	14A	8A	12A
	output power (W)	7kW	4kW	6kW
Average SM capacitor voltage $Vc1, Vc2, Vc3$ for each phase		64V	61.5V	62.5V
M-MC side active power output		6.6kW	3.65kW	5.4 kW
Grid side active power output		1.6kW	1.35kW	400W
Load side active power output		5kW	5kW	5kW

5. Conclusion

The feasibility of an M-MC topology as an interface between the grid and PEMFC with an efficient control algorithm has been simulated (with real-time simulation using OP-5700 simulator) and the performance has been analysed in this paper. The boost converter controls and conditions the fuel cell's output power. In the case of changes in hydrogen flow rate, load, or fuel cell operating conditions, the PI controller adjusts the converter's MPPT duty ratio to deliver the best possible output voltage. The SM capacitor voltages are balanced, with a peak voltage ripple of 12.5% from the DC bus voltage regulation, which is the same as at the base frequency. There is a substantial reduction in voltage fluctuation, and the voltages are in a reasonable profile and well balanced. The harmonics of the circulating current have a peak value of about 30% of the peak arm current. As a result of the reduction in distortion, a pure sinusoidal arm current waveform is obtained. Using the analytical solution for a M-MC configuration, it has been identified that the THD value for M-MC phase voltage is 1.89%, the grid current is 2.67% and the M-MC arm current is 4.01%. The THD is observed to be the almost same and is lower than 5% which is under IEEE standards. For the sudden changes in PEMFC temperature at different operating conditions, ac & dc voltage, current and active power variations are obtained and validated. The control system of the 6kW PEMFC based grid-connected M-MC configuration with the designed parameters under different operating temperature is successfully analysed.

References

[1] Abdelhakim Belkaid, Ilhami Colak, Korhan Kayisli, and Ramazan Bayindir, "Design and Implementation of a Cuk Converter Controlled by a Direct Duty Cycle INC-MPPT in PV Battery System | Belkaid | International Journal of Smart Grid - ijSmartGrid," Int. J. Smart Grid, vol. 3, no. 1, pp. 19–25, 2019.

[2] I. Yaichi, A. Semmah, and P. Wira, "Direct power control of a wind turbine based on doubly fed induction generator," European Journal of Electrical Engineering, vol. 21, no. 5, pp. 457–464, 2019, doi: 10.18280/ejee.210508.

[3] M. Caruso, R. Miceli, P. Romano, G. Schettino, and F. Viola, "Technical and Economical Performances of Photovoltaic Generation Facades," Int. J. Smart grid, vol. 2, no. 2, 2018, doi: 10.20508/ijsmartgrid.v2i2.19.g19.

[4] B. Sørensen and G. Spazzafumo, "Introduction," Hydrog. Fuel Cells, pp. 1–4, 2018, doi: 10.1016/b978-0-08-100708-2.00001-1.

[5] S. F. Jaber and A. M. Shakir, "Design and Simulation of a Boost-Microinverter for Optimized Photovoltaic System Performancec," Int. J. Smart grid, vol. 5, no. 2, 2021, doi: 10.20508/ijsmartgrid.v5i2.189.g145.

[6] M. İnci and Ö. Türksoy, "Review of fuel cells to grid interface: Configurations, technical challenges and

trends," J. Clean. Prod., vol. 213, pp. 1353–1370, 2019, doi: 10.1016/j.jclepro.2018.12.281.

[7] K. Ahmed, O. Farrok, M. M. Rahman, M. S. Ali, M. M. Haque, and A. K. Azad, "Proton Exchange Membrane Hydrogen Fuel Cell as the Grid Connected Power Generator," Energies, vol. 13, no. 24, p. 6679, 2020, doi: 10.3390/en13246679.

[8] B. Zafar, "Design of a Renewable hybrid photovoltaic-Electrolyze-PEM/Fuel Cell System using Hydrogen Gas," Int. J. Smart grid, vol. 3, no. 4, 2019, doi: 10.20508/ijsmartgrid.v3i4.83.g68.

[9] M. İnci, M. Büyük, M. H. Demir, and G. İlbey, "A review and research on fuel cell electric vehicles: Topologies, power electronic converters, energy management methods, technical challenges, marketing and future aspects," Renew. Sustain. Energy Rev., vol. 137, no. December 2020, 2021, doi: 10.1016/j.rser.2020.110648.

[10] F. Sergi, G. Brunaccini, A. Stassi, A. Di Blasi, G. Dispenza, A.S. Arico`, M. Ferraro, V. Antonucci, "PEM fuel cells analysis for grid connected applications," Int. J. Hydrogen Energy, vol. 36, no. 17, pp. 10908–10916, 2011, doi: 10.1016/j.ijhydene.2011.05.161.

[11] H. Abu-Rub, J. Holtz, J. Rodriguez, and Ge Baoming, "Medium-Voltage Multilevel Converters—State of the Art, Challenges, and Requirements in Industrial Applications," IEEE Trans. Ind. Electron., vol. 57, no. 8, pp. 2581–2596, 2010, doi: 10.1109/TIE.2010.2043039.

[12] A. Lesnicar and I. Introduction, "An Innovative Modular Multilevel Converter Topology Suitable for a Wide Power Range," 2003.

[13] C. Buccella, M. G. Cimoroni, C. Cecati, L. A. Disim, and L. Aquila, "Low-Frequency Harmonic Elimination Technique in Cascaded H-Bridges Multilevel Inverters for Renewable Energy Applications," Int. J. Smart grid, vol. 3, no. 1, pp. 1–9, 2019, doi: 10.20508/ijsmartgrid.v3i1.41.g39.

[14] Z. Liu, S. Miao, Z. Fan, K. Chao, and Y. Liu, "Characteristics analysis and improved arm control of modular multilevel converter under asymmetric operation conditions," Int. J. Electr. Power Energy Syst., vol. 105, no. May 2018, pp. 272–282, 2019, doi: 10.1016/j.ijepes.2018.08.037.

[15] M. F. Masood, M. I. Abid, M. S. Khalid, M. A. Rasheed, H. U. Rehman, and T. Zahid, "A Novel Solution to Eliminate Frequency Intermittency by Adding Spinning Reserve to the Micro-Hydro Turbine Generator using Real-Time Control of Induction Motor through AC-DC-AC Power Converters," Int. J. Smart grid, vol. 4, no. 4, 2020, doi: 10.20508/ijsmartgrid.v4i4.120.g106.

[16] N. Rasekh and M. Hosseinpour, "LCL filter design and robust converter side current feedback control for grid-connected Proton Exchange Membrane Fuel Cell system," Int. J. Hydrogen Energy, vol. 45, no. 23, pp. 13055–13067, 2020, doi: 10.1016/j.ijhydene.2020.02.227.

[17] Y. Zhan, Y. Guo, J. Zhu, B. Liang, and B. Yang, "Comprehensive influences measurement and analysis of power converter low frequency current ripple on PEM fuel cell," Int. J. Hydrogen Energy, vol. 44, no. 59, pp. 31352–31359, 2019, doi: 10.1016/j.ijhydene.2019.09.231.

[18] F. Shahnazian, J. Adabi, E. Pouresmaeil, and J. P. S. Catalão, "Interfacing modular multilevel converters for grid integration of renewable energy sources," Electr. Power Syst. Res., vol. 160, pp. 439–449, 2018, doi: 10.1016/j.epsr.2018.03.014.

[19] Z. Ou, G. Wang, and L. Zhang, "Modular Multilevel Converter Control Strategy Based on Arm Current Control Under Unbalanced," vol. 33, no. 5, pp. 3826–3836, 2018.

[20] Y. Wang, C. Zhao, and C. Guo, "Comparison study of small-signal stability of MMC-HVDC system in different control modes," Int. J. Electr. Power Energy Syst., vol. 111, no. August 2018, pp. 425–435, 2019, doi: 10.1016/j.ijepes.2019.04.017.

[21] A. Nami, J. Liang, F. Dijkhuizen, and G. D. Demetriades, "Modular multilevel converters for HVDC applications: Review on converter cells and functionalities," IEEE Trans. Power Electron., vol. 30, no. 1, pp. 18–36, 2015, doi: 10.1109/TPEL.2014.2327641.

[22] H. Nademi, L. Norum, and A. Das, "A New Circuit of Modular Multilevel Inverter for Grid-Connected Photovoltaic Conversion Plants," no. 1, 2015.

[23] J. Mei, B. Xiao, K. Shen, L. M. Tolbert, and J. Y. Zheng, "Modular multilevel inverter with new modulation method and its application to photovoltaic grid-connected generator," IEEE Trans. Power Electron., vol. 28, no. 11, pp. 5063–5073, 2013, doi: 10.1109/TPEL.2013.2243758.

[24] F. Odeim, J. Roes, L. Wülbeck, and A. Heinzel, "Power management optimization of fuel cell/battery hybrid vehicles with experimental validation," J. Power Sources, vol. 252, pp. 333–343, 2014, doi: 10.1016/j.jpowsour.2013.12.012.

[25] C. B. Robledo, V. Oldenbroek, F. Abbruzzese, and A. J. M. van Wijk, "Integrating a hydrogen fuel cell electric vehicle with vehicle-to-grid technology, photovoltaic power and a residential building," Appl. Energy, vol. 215, no. January, pp. 615–629, 2018, doi: 10.1016/j.apenergy.2018.02.038.

[26] S. Farhani, A. N'Diaye, A. Djerdir, and F. Bacha, "Design and practical study of three phase interleaved boost converter for fuel cell electric vehicle," J. Power Sources, vol. 479, no. June, p. 228815, 2020, doi: 10.1016/j.jpowsour.2020.228815.

[27] M. A. Soumeur, B. Gasbaoui, O. Abdelkhalek, J. Ghouili, T. Toumi, and A. Chakar, "Comparative study of

energy management strategies for hybrid proton exchange membrane fuel cell four wheel drive electric vehicle," J. Power Sources, vol. 462, no. April, p. 228167, 2020, doi: 10.1016/j.jpowsour.2020.228167.

[28]   K. J. Reddy and N. Sudhakar, "ANFIS-MPPT control algorithm for a PEMFC system used in electric vehicle applications," Int. J. Hydrogen Energy, vol. 44, no. 29, pp. 15355–15369, 2019, doi: 10.1016/j.ijhydene.2019.04.054.

[29]   N. Benyahia , H. Denoun, A. Badji , M. Zaouia , T. Rekioua , N. Benamrouche , D. Rekioua ., "MPPT controller for an interleaved boost dc-dc converter used in fuel cell electric vehicles," Int. J. Hydrogen Energy, vol. 39, no. 27, pp. 15196–15205, 2014, doi: 10.1016/j.ijhydene.2014.03.185.

[30]   A. Haddad, M. Mannah, and H. Bazzi, "Nonlinear time-variant model of the PEM type fuel cell for automotive applications," Simul. Model. Pract. Theory, vol. 51, pp. 31–44, 2015, doi: 10.1016/j.simpat.2014.11.002.

[31]   K. Jyotheeswara Reddy and N. Sudhakar, "A new RBFN based MPPT controller for grid-connected PEMFC system with high step-up three-phase IBC," Int. J. Hydrogen Energy, vol. 43, no. 37, pp. 17835–17848, 2018, doi: 10.1016/j.ijhydene.2018.07.177.

[32]   A. Harrag and S. Messalti, "How fuzzy logic can improve PEM fuel cell MPPT performances?," Int. J. Hydrogen Energy, vol. 43, no. 1, pp. 537–550, 2018, doi: 10.1016/j.ijhydene.2017.04.093.

[33]   H. Akagi, "Classification, terminology, and application of the modular multilevel cascade converter (MMCC)," IEEE Trans. Power Electron., vol. 26, no. 11, pp. 3119–3130, 2011, doi: 10.1109/TPEL.2011.2143431.

[34]   R. K, S. N. R, B. K. K, and S. R. Y, "Efficient modeling and simulation of grid connected MMC for sustainable photovoltaic and wind conversion system," Sustain. Comput. Informatics Syst., vol. 28, p. 100402, 2020, doi: 10.1016/j.suscom.2020.100402.

[35]   S. Du, A. Dekka, B. Wu, and N. Zargari, "FUNDAMENTALS OF MODULAR," pp. 37–78.

[36]   S. Du, A. Dekka, B. Wu, and N. Zargari, "General Aspects of Conventional MMC," Modul. Multilevel Convert. Anal. Control. Appl., 2018, doi: 10.1002/9781119367291.ch1.

[37]   T. Demirdelen, R. Kayaalp, and M. Tumay, "Simulation modelling and analysis of modular cascaded multilevel converter based shunt hybrid active power filter for large scale photovoltaic system interconnection," Simul. Model. Pract. Theory, vol. 71, pp. 27–44, 2017, doi: 10.1016/j.simpat.2016.11.003.

[38]   K. K. Gupta, A. Ranjan, P. Bhatnagar, L. K. Sahu, and S. Jain, "Multilevel inverter topologies with reduced device count: A review," IEEE Trans. Power Electron., vol. 31, no. 1, pp. 135–151, 2016, doi: 10.1109/TPEL.2015.2405012.

[39]   A. B. Rey-boué, F. Martinez-rodrigo, N. F. Guerrero-rodríguez, L. C. H. Lucas, and S. De Pablo, "Enhanced controller for grid-connected modular multilevel converters in distorted utility grids," Electr. Power Syst. Res., vol. 163, no. July, pp. 310–327, 2018, doi: 10.1016/j.epsr.2018.06.011.